John P. Swensen[1]
Mem. ASME
Department of Mechanical Engineering and Materials Science,
Yale University,
9 Hillhouse Ave., Mason Lab 110,
New Haven, CT 06511
e-mail: john.swensen@yale.edu

Lael U. Odhner
Right Hand Robotics LLC,
Medford, MA 02155
e-mail: lael@righthandrobotics.com

Brandon Araki
Massachusetts Institute of Technology,
Cambridge, MA 02139
e-mail: br.araki@gmail.com

Aaron M. Dollar
Mem. ASME
Department of Mechanical Engineering and Materials Science,
Yale University,
15 Prospect Street,
New Haven, CT 06520
e-mail: aaron.dollar@yale.edu

Printing Three-Dimensional Electrical Traces in Additive Manufactured Parts for Injection of Low Melting Temperature Metals

While techniques exist for the rapid prototyping of mechanical and electrical components separately, this paper describes a method where commercial additive manufacturing (AM) techniques can be used to concurrently construct the mechanical structure and electronic circuits in a robotic or mechatronic system. The technique involves printing hollow channels within 3D printed parts that are then filled with a low melting point liquid metal alloy that solidifies to form electrical traces. This method is compatible with most conventional fused deposition modeling and stereolithography (SLA) machines and requires no modification to an existing printer, though the technique could easily be incorporated into multimaterial machines. Three primary considerations are explored using a commercial fused deposition manufacturing (FDM) process as a testbed: material and manufacturing process parameters, simplified injection fluid mechanics, and automatic part generation using standard printed circuit board (PCB) software tools. Example parts demonstrate the ability to embed circuits into a 3D printed structure and populate the surface with discrete electronic components. [DOI: 10.1115/1.4029435]

1 Introduction

Rapid fabrication processes such as SLA and fused deposition modeling (FDM) have had a profound impact in many domains, including the production of robotic and mechatronic systems. While this impact has been, to date, primarily within the research domain, the build quality and robustness of systems produced using AM techniques is beginning to allow for commercial grade systems to be produced. When best-practice design rules are followed (e.g., Refs. [1] and [2]), high-quality hardware that might take weeks to fabricate by conventional computer numerical control (CNC) machining processes can be made in days or even hours at a fraction of the cost. This gives researchers an unprecedented ability to iteratively redesign robots based on experiments and also enables the open publication of complete hardware designs in an easily reproducible form [3–5].

Traditionally, electronics for robotics and mechatronics has been done using standard prototyping boards or commercially manufactured PCBs. And while there are well-developed processes and design tools for the generation of circuits using these traditional methods, the integration with hardware is almost always done through mounting of the circuit board to the robot hardware and associated cabling during robot assembly. A next frontier in rapid fabrication in these domains is electronic integration. Although processes such as shape deposition manufacturing have been used to create robots with embedded sensors and actuators [6,7], techniques for rapid fabrication of integrated electronics are nowhere near as refined and user-friendly as those for creating mechanisms. For example, the fingers of the iRobot–Harvard–Yale (iHY) hand have low-cost encoders, accelerometers, and contact sensors [8,9], but the process for the integration of electronic components consists of inserting a prefabricated circuit with wiring into a mold before epoxy is cast. In processes such as this, the electrical system is separately prefabricated, and care must be taken to ensure that components are placed properly within the mold throughout the entire fabrication process.

In this paper, we describe a method of creating a three-dimensional circuit layout directly within the 3D printed part using hollow channels, Fig. 1(*c*), and then depositing conductors directly into those by injecting a low melting temperature metal that hardens when cool, as seen in Fig. 1(*b*). Along with the fabrication process, we also describe a way to use existing circuit design tools, such as a typical board layout shown in Fig. 1(*a*), to automatically generate the 3D CAD model of a part with the equivalent channels ready for injection. Prior to injecting the metal conductors, the surface of the part is populated with the discrete electronic components, which are then connected and held in place when the conductor hardens. Thus, the part made through the AM process serves as both the structural component and the PCB. We demonstrate this concept within parts produced on a commercial FDM printer with subsequent injection of liquid metal into channels within the 3D printed parts, but the process is compatible with many commercial AM processes and does not require modification of the machine itself. Though all the fabrication discussed in this paper addresses standard through-hole components, the method could potentially be extended to work with surface mount components through careful engineering of the surface geometry where the injected metal exits the part.

The remainder of this paper is broken into several sections. First, in Sec. 2, we provide a comprehensive review of related work. In Sec. 3, an overview of available materials and techniques for rapid fabrication of circuits is presented, in conjunction with the available design parameters for liquid metal injection. Section 4 lays out the process parameters for liquid metal injection of circuits and the mechanics associated with the travel of liquid metal along channels during injection. Then, Sec. 5 describes the tools and algorithms used to automatically generate the 3D model of the circuit from standard design tools. Section 6 discusses several experiments comparing the theory discuss in Sec. 4 with experimental results concludes with two example parts that demonstrate

[1]Corrresponding author.

Contributed by the Mechanisms and Robotics Committee of ASME for publication in the JOURNAL OF MECHANISMS AND ROBOTICS. Manuscript received September 2, 2014; final manuscript received December 12, 2014; published online February 27, 2015. Assoc. Editor: Satyandra K. Gupta.

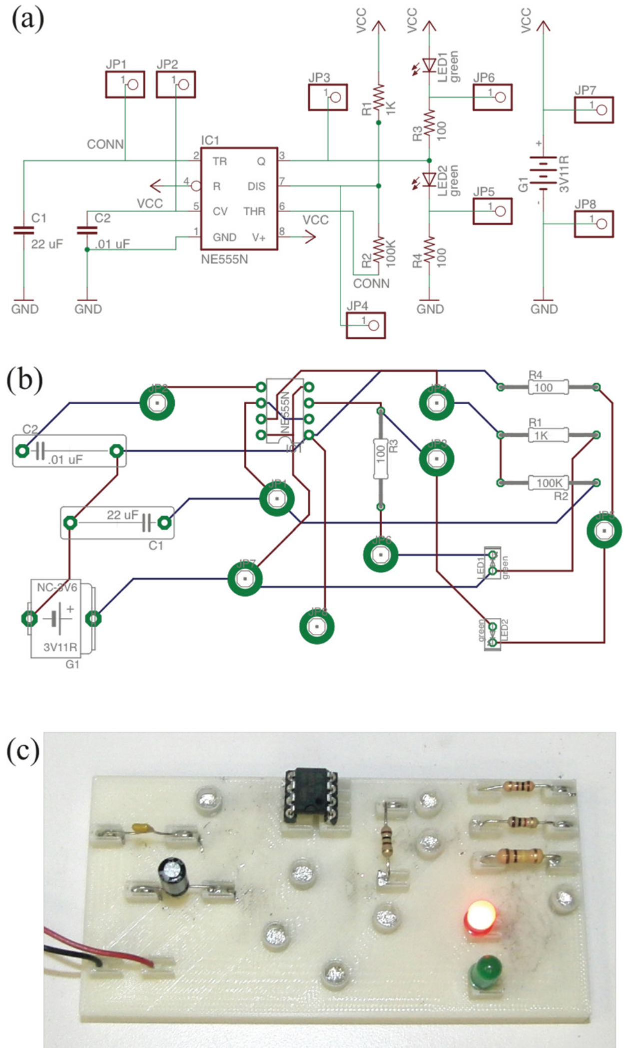

Fig. 1 The process of creating circuits by designing hollow channels in 3D printed parts and injecting with low melting point metals to create complete electrical traces: (*a*) a schematic capture of a 555 timer circuit, (*b*) a PCB board layout for the timer circuit, and (*c*) an operating circuit after injection

the features of the liquid metal injection technique. Section 7 concludes with a discussion of future directions for development.

2 Related Work

The creation of circuits using AM processes is a rapidly evolving research area, and one in which the functional requirements vary significantly depending on the precise niche application. In this section, we review both methods of printing conductive structures and materials as well as materials commonly used to create 3D printed circuits.

Conductive Composites. Slurries and composites, such as carbon nanofiber epoxies [10], carbon black composites [11], and conductive silicone [12], have been used to create 3D printed conductive traces. Although epoxies and composites are well suited for extrusion by a 3D printer, they are often either relatively expensive or difficult to make, require long curing times or special curing agents, and have relatively high resistivity.

Conductive Inks and Paints. Conductive paints (such as bare paint [13]) are popular among hobbyists for being cheap and nontoxic; however, their high resistivity (2.75 Ω mm) means that circuits for sensors and antennae cannot be made without using large trace dimensions. Silver nanoparticle ink can be deposited by an inkjet printer to create precise, highly detailed circuits quickly and easily. However, the rate of deposition is limited and it is difficult to build up thick traces, so current through the traces is limited [14]. In addition, since the substrate must be absorptive and some processes require sintering temperatures of up to 200 °C [15], inkjet technologies are unsuited for most 3D-printed plastics. Moreover, these inkjet-printed circuits are limited to two-dimensional geometries.

Metals. Free-standing microstructures composed of liquid metal beads have been created using a 3D printer with a specialized extruder [16]. This method shows promise for printing small, conductive 3D structures; however, the high surface tension of liquid metal limits the control that can be exerted over the geometry of the structures that can be produced. The surface tension problem can be solved by injecting liquid metal into already-formed structures; eutectic gallium indium alloy has also been directly injected into traces in polydimethylsiloxane (PDMS) to make two-dimensional stretchable, flexible circuits [17]. Although liquid traces such as these would be difficult to keep in place long term with an FDM part due to their porosity, this work is a good example of high-conductivity, geometrically structured circuit traces, and significant ideas have been adapted for the present work. Siegel et al. [18] proposed methods of generating arbitrary 3D shapes of solder by injecting liquid solder into PDMS microchannels, deforming the PDMS structure while the metal is liquid, then cooling to harden the solder in the desired shape. The proposed technique could be used for circuits, sensors, and other integrated electronics. Dickey et al. [19] developed models of the flow of room-temperature liquid EGaIn metals into microchannels in PDMS under various pressure conditions.

Rapid Prototyping (RP) Circuit Methods. Early work on rapidly prototyped circuits consisted mostly of depositing capacitors or resistors directly onto PCB [20]. Later, pioneering work in multimaterial printing, where the secondary material was conductive silicone, was done by Periard et al. [12]. This work allowed the circuit to be embedded within the 3D printed part. More recent work has developed a variety of methods for printing circuits on the surface of rapid-prototyped parts, using either conductive SLA materials or filling the channels as a postprint step [21–24]. This most recent work was limited to single layer circuits and utilize multiple interlocking parts or multiple faces of the part to implement more complex circuits that could not be achieved with a single layer.

The work presented in this paper provides an alternative to the existing methods, which has the added benefit in which it can (1) be used with existing single-material SLA and FDM printer through a postprint injection step, (2) accommodate multilayer circuit designs, (3) can be embedded anywhere in the part with only the discrete component on the surface of the part, and (4) circuits can be generated using traditional circuit design tools and automatic conversion to the RP circuit is presented.

3 Process Overview

The process for creating injected metal circuits is diagrammed in Fig. 2. First, a series of small channels are designed into a solid part and printed on a FDM printer. These channels are each connected to a single sprue (or injection point) used to fill the channel. Any electrical components making a connection with the channels are inserted through connected holes on the surface of the part. The injection apparatus consists of a syringe pump, syringe, reservoir of liquid metal, two check valves, tubing, and the industry standard slip tip tube fitting. The first bidirectional check valve allows the syringe in the pump to draw in liquid metal when retracting and to infuse liquid to the circuit when moving forward.

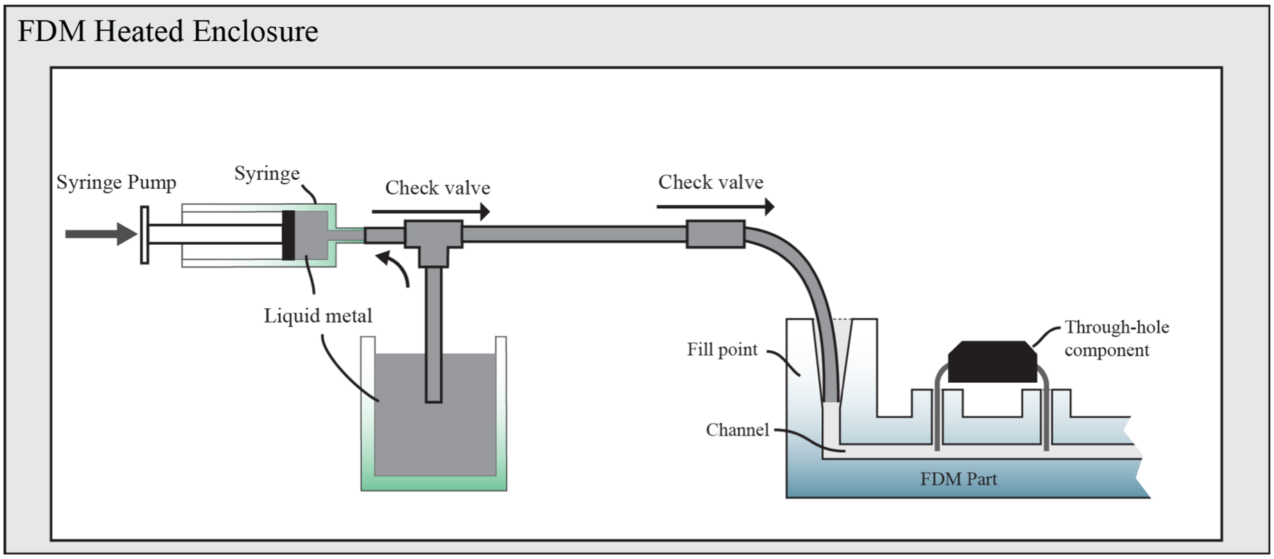

Fig. 2 A schematic of the integrated wiring process, including the syringe pump, reservoirs, checks valves, and printed channels into which liquid metal is injected. Each trace within the part has a sprue, or injection point, used to fill the trace and the outlet of the injection device seals into the injection port using standard slip tip syringe connectors. The check valve ensures that the injection pathway remains primed with liquid metal between injections.

The second check valve only allows forward pumping so as to keep the tubing primed with the liquid metal.

During infusion, the metal flows through the injection point, fills the channels until reaching the electrical connections at the surface, and then is removed from the heated enclosure to cool and harden the traces. The hardened traces also act as a solder holding inserted components in place and creating electrical connection with component pins. Many of the process parameters involved in this fabrication process must be carefully chosen if it is to work correctly. Material choice, trace sizing, and component insertion are all affected by a variety of other factors—for example, operating temperature, material properties, and printer settings. This section analyzes the most critical design parameters and provides guidelines that produce repeatable results.

All injections are conducted with an NE-510 syringe pump (New Era Pump Systems, Inc., Farmingdale, NY) which is capable of providing a constant injection rate between 8.349 μl/hr and 607.6 μl/hr using a 10 ml syringe. This model is able to exert 444.8 N at stall and 80.1 N at top speed. These extremely high forces allow us to develop the simplified fluid mechanics model in Sec. 4 by assuming that the injection apparatus can deliver the necessary pressures to provide a constant injection flow rate.

3.1 Choice of Alloy. The choice of metal for wiring is heavily constrained by the thermal material properties of both the metal and the rapid-prototyped parts, as well as the temperature at which injection takes place and the operating temperature of the circuit. The metal must be liquid at a temperature that the printed parts can withstand, but must also solidify at a high enough temperature to be reliably solid at room temperature and when running acceptable amounts of current through the solidified wires. The upper temperature bound was chosen based on the properties of acrylonitrile butadiene styrene (ABS), the plastic most commonly used in FDM printers. This plastic never melts but becomes soft at its glass transition temperature of 108 °C [25]. The lower bound of the desired metal melting point was chosen to be 50 °C, which is sufficiently far above room temperature that a wire carrying limited current should never melt. Most of the commercially available metals that melt in this range are not pure metals, but eutectics-alloys having the special property of melting at a single temperature rather than gradually melting over a range of temperatures. Of these eutectic mixtures, many are unsuitable because they include highly toxic metals, most notably cadmium.

We chose to use Cerrolow 136, a eutectic mixture of bismuth (49%), indium (21%), lead (18%), and tin (12%) [26]. This alloy melts at 57.8 °C and contains less lead than many of the alternative choices. Cerrolow 136 also has the desirable property of having almost no net volume change (0.0023%/°C) as it solidifies. This is useful because it does not have a tendency to warp and deform the parts as it cools, or to crack or bubble, creating breaks in the traces. There are a variety of other low melting points, and sometimes eutectic, metals such as Rose's metal, Wood's metal, or Field's metal. Each of these alternatives has advantages and disadvantages: Field's metal does not contain lead but is 51% indium making it very costly, whereas Rose's metal has a much higher melting point, and Wood's metal contains the highly toxic cadmium. Our choice of Cerrolow 136 minimized cost and is safe through handling of circuits and materials with the lead content in mind.

Cerrolow 136 has a resistivity of 7.081×10^{-7} Ω m, which is higher than copper (1.68×10^{-8} Ω m) but typical of many solders ($\sim 1.45 \times 10^{-7}$ Ω m), and certainly much lower than many carbon-polymer composites [10–12]. A 0.8 mm × 0.8 mm trace, equivalent in area to a 19 American Wire Gauge (AWG) copper wire, has approximately the same resistance per meter as copper wire between 35 and 36 AWG

$$\frac{R}{L} = \frac{\rho}{A} = \frac{7.081 \times 10^{-7}}{6.4 \times 10^{-7}} = 1.11 \frac{\Omega}{\text{m}} \tag{1}$$

where R is resistance, L is the length of the conductor, ρ is the conductivity of the Cerrolow 136, and A is the cross-sectional area of the conductor. Such a wire is rated by the National Fire Protection Association at between 0.21 and 0.27 A continuous load [27], which is sufficient for supplying power to sensors, microprocessors, and other discrete components, as well as power to small motors. It is important to note, however, that amperage ratings are given for conductors with a thin insulator exposed to air, whereas these wires are embedded in block of RP material, so designers should be conservative when determining allowable current and channel diameters. A series of test pieces are described in Sec. 5 which verify that given a designed cross-sectional area and length of conductor that the resistance is quite near to that calculated using Eq. (1).

3.2 Trace Size and Spacing. The size of the traces used in the parts is partially governed by the size of the channels that can be printed into parts via FDM, and partially governed by the properties of the liquid metal used. The minimum feature size on a commercial grade FDM printer is 0.36–0.63 mm, and it was experimentally determined on the authors' Fortus 250mc (Stratasys, MN) that channels smaller than 0.8×0.8 mm^2 exhibited occasional blockages due to unpredictable print irregularities and variability in actual dimension. For reliability, a minimum of 0.8×0.8 mm^2 profile and a maximum of 1.6×1.6 mm^2 profile were used throughout all experiments. Figure 3 shows that two different potential channel profiles with respect to the manner in which FDM layers are deposited. Most FDM printers allow a nominal amount of overhang before it requires support material to fill in the gap left by a void. At the larger 1.6×1.6 mm^2 channel size, the square channel on the left in Fig. 3 would require support material. No support material would be required regardless of channel size for the diamond shaped channel shown on the right of Fig. 3. Support material in FDM printers is often dissolvable in a lye bath, but due to the extremely small size of the channels, it would be difficult to ensure that the support material has been completely removed. As such, channel geometries that would require support material are avoided and the diamond shape is used through all experiments.

The spacing between traces was bounded from below by the tendency of the liquid metal to leak between channels, and consequently creates a short circuit, if the separation becomes too small. To avoid this, the circuit channels were spaced at twice the maximum feature size, so that two contours of solid ABS lay between them (approximately 1 mm under nominal settings on a Stratasys Fortus 250). When possible, four contours were used to further prevent leakage between channels. Figure 4 depicts the spacing used, where the shaded region represents the deposited contours with two channels on either side.

3.3 Injection and Venting. Both the syringe full of liquid metal and the printed part must be fully above 57.8 °C, in order to ensure that the injection process is reliable. Otherwise, the liquid metal can solidify midway through the infusion of a trace, causing a blockage, and a failure to reach all components connected to the trace. In practice, an excellent way to accomplish this is to keep both the syringe and the printed part in the heated enclosure of the 3D printer during injection. Most commercial printers hold their enclosures at 75 °C. If each outlet at a component pin is properly vented, a small amount of material should be visible at the completion of the injection process. If any blockage occurs during injection, whether due to solidification due to cooling or due to a print error, the possibility of leakage increases due to the semiporous nature of FDM and the increase in pressure may be sufficient to force the liquid metal through small features that would not appear porous at lower pressures. While we used the enclosure of the 3D printer to attain sufficiently high temperature, an oven or heating plate could also be used to maintain the appropriate temperature of the metal and the part.

When multiple traces branch out from a single injection point, it is crucial that the ends of each branch be properly vented to allow air to escape. This is usually accomplished by making sure that the holes in which components are inserted are loosely fit around the component pins or wires. For standard through-hole components, our outlet holes were always 1.0 mm^2. It is also usually a good idea to avoid large differences in length between branches of the trace, as short branches may then overflow and leave long branches unfilled. The injection point may need to be judiciously placed to accomplish this. Section 3 presents models and simulations for injections including branching based on the volumetric flow rate down each branch, and Sec. 4 presents an algorithm for determining the appropriate cross-sectional area of each channel segment to ensure that the advancing liquid metal reaches all of the vents and component pins simultaneously, thus eliminating spillage.

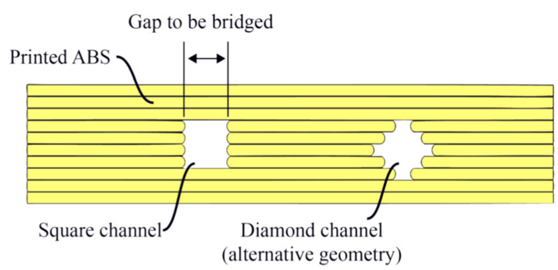

Fig. 3 Channels for electrical traces were made using square profiles in the printed parts. To avoid printing support material into the traces, a diamond-shaped channel may be necessary.

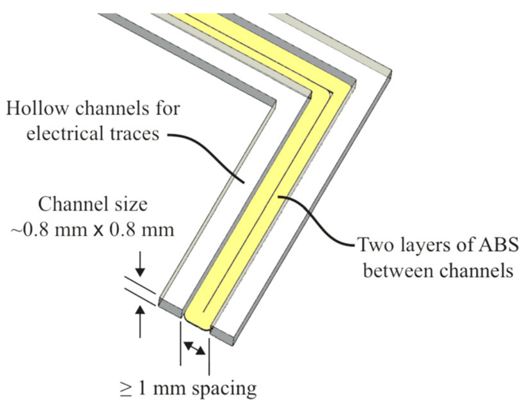

Fig. 4 The channels must be spaced so that two widths of the printed ABS filament can fit between them

3.4 Summary. This section has presented the primary design considerations for both RP material and injection metal for the proposed method of injecting liquid metal into channels in the RP part. It also identified the choices made based on heuristics from the authors' FDM printer and testing of various metals. Other types of printer (for example, SLA or FDM with Nylon) can be used, as long as it is possible to make long hollow channels within printed parts. When the thermal properties of these other materials are different, other design choices may need to made, such as choosing an injectable metal with a different melting point.

4 Injection Fluid Mechanics

One of the key objectives for the liquid metal injection is to do a single injection for each portion of the circuit that has equivalent electrical potential (a "node voltage" in circuit terminology) such that the liquid metal reaches the outlet at the pins of the discrete components simultaneously. This limits spillage at the surface of the part and reduces the likelihood of shorts between traces due to spillage. In order to attempt this goal, factors such the volumetric flow rate of the injected metal, the length and diameter of each channel, and the topology of the branching channels from injection to vent must be considered.

A simplified model for the advancing fluid is given by the Hagen–Poiseuille equation, which describes the relationship between the pressure drops in a fluid flowing through a cylindrical pipe

$$\Delta P = \frac{128\mu L}{\underbrace{\pi d^4}_{R}} Q \tag{2}$$

where μ is the dynamic viscosity in Pa s, d is the channel diameter in meters, L is the fluid length in meters, and Q is the volumetric flow rate in m^3/s. The entire term R can be thought of as the fluid flow resistance. That is, the pressure drop along the channel is function of the resistance to flow (dependent on fluid material properties and channel geometry) and the volumetric flow rate. The average fluid velocity can be computed from the volumetric flow rate as

$$V_{\mathrm{ave}} = \frac{Q}{A} = \frac{4}{\pi d^2} Q \tag{3}$$

For an advancing fluid head, the length of the liquid metal inside the channel is then a function of time, the fluid material properties, the channel geometry, and the volumetric flow rate

$$L(t) = \int_0^t V_{\mathrm{ave}} d\tau = V_{\mathrm{ave}} \tau |_0^t = \frac{4}{\pi d^2} Q t \tag{4}$$

And while the use of the Hagen–Poiseuille equation describes the flow of fluid in a single channel with advancing fluid, in the proposed method for RP circuit creation there are multiple branches of the channels and a model of fluid behavior must be derived for arbitrary branching.

At this point, several simplifying assumptions are made to the model: (1) any oxidization and other effects that occurs at the advancing fluid front that may cause the fluid advancement to not be accurately described by the Hagen–Poiseuille equation are neglected, (2) pressure drops that occur at branching junctions and at changes in the channel diameter are neglected, (3) the pressure drop between the advancing fluid and the outlet of the trace is neglected due to the fact that the pressure drop due to the ambient air is orders of magnitude less than the pressure drop in the fluid because of the difference in viscosity between the metal and the air, and (4) it is assumed that the syringe pump pushing liquid medal into the channels can exert sufficient force to keep the incoming volumetric flow rate constant regardless of the back pressure. These simplifications could be relaxed in future work, but in the work presented herein these assumptions allow for the channel diameter optimization described in the subsequent section to ensure that the fluid reaches the component pins on the surface of the part almost simultaneously.

Using these assumptions, the relative volumetric flow rate down each of the channels at a branch point can be computed based on the resistance to fluid flow exhibited by each of the channels. Figure 5 shows the advancing fluid flow at two different points in time for a series of branching channels. In Fig. 5(*a*), the fluid flow in each of the channel splitting from the main channel would be

$$Q_2 = \frac{R_3}{R_2 + R_3} Q_1 \text{ and } Q_3 = \frac{R_2}{R_2 + R_3} Q_1 \tag{5}$$

In general, the flow down the kth channel, Q_k can be computed as

$$Q_k = \frac{R_{\mathrm{T}}}{R_k + R_{\mathrm{T}}} Q_{\mathrm{in}} \tag{6}$$

where R_k is the fluid flow resistance of the kth channel, R_{T} is the parallel equivalent fluid flow resistance of all other channel from the branch point, and Q_{in} is the volumetric flow rate coming into the branch point. Thus, as an example, the volumetric flow rate Q_3 in Fig. 5(*b*) would be

$$Q_3 = \frac{R_2 + R_4 || R_5}{R_3 + R_2 + R_4 || R_5} Q_1 \tag{7}$$

with parallel fluid flow resistance computed as

$$R_i || R_j = \frac{1}{\frac{1}{R_i} + \frac{1}{R_j}} \tag{8}$$

Experiments comparing simulated fluid flow rates with those from actual injections are presented in Sec. 5.

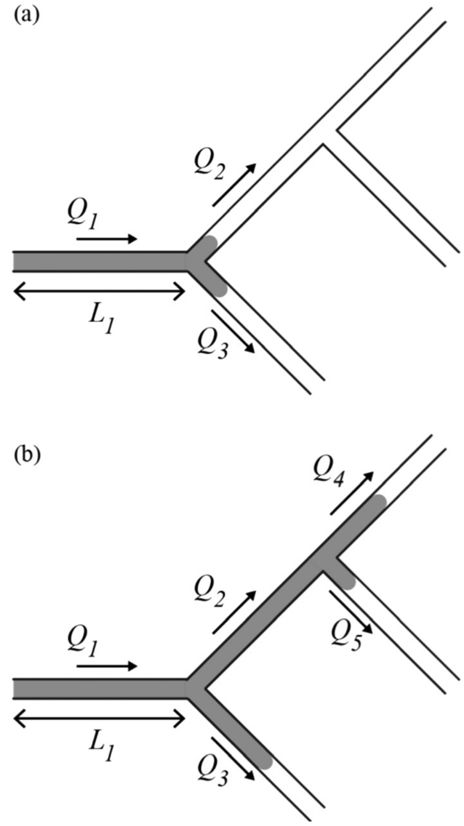

Fig. 5 The advancing fluid flow with branching where the branching flow is determined by relative fluid flow resistance in each channel: (*a*) the first branch point has been reached and (*b*) multiple branches have occurred

5 Circuit Generation Automation

Traditionally, PCBs are designed in specialized computer aided design (CAD) software. In software such as EAGLE PCB (CadSoft, Inc., FL) or ORCAD (Cadence Design Systems, Inc., CA), this is done as a three step process consisting of (1) schematic capture, (2) board layout, and (3) postprocessing of board layout to generate layers, masks, and drill holes. To facilitate the generation of rapidly prototyped circuits using the principles and techniques described in Secs. 2 and 3, an automated procedure to generate 3D printable parts with the embedded circuit in standard tessellation language (STL) format was devised. This MATLAB (The Mathworks, Inc., MA) software took the output of step 2 above, a .BRD file from the EAGLE PCB and generated the corresponding STL file representing the circuit.

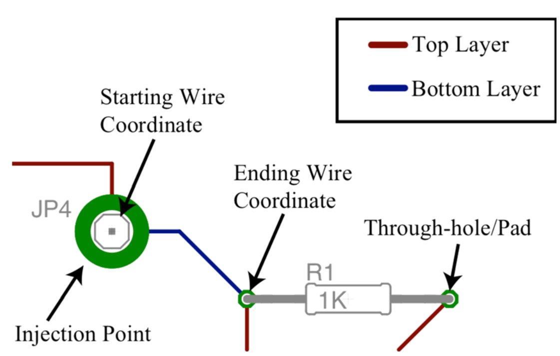

Fig. 6 A diagram of the types of circuit elements that must be converted from the layered PCB format to an equivalent three-dimensional representation

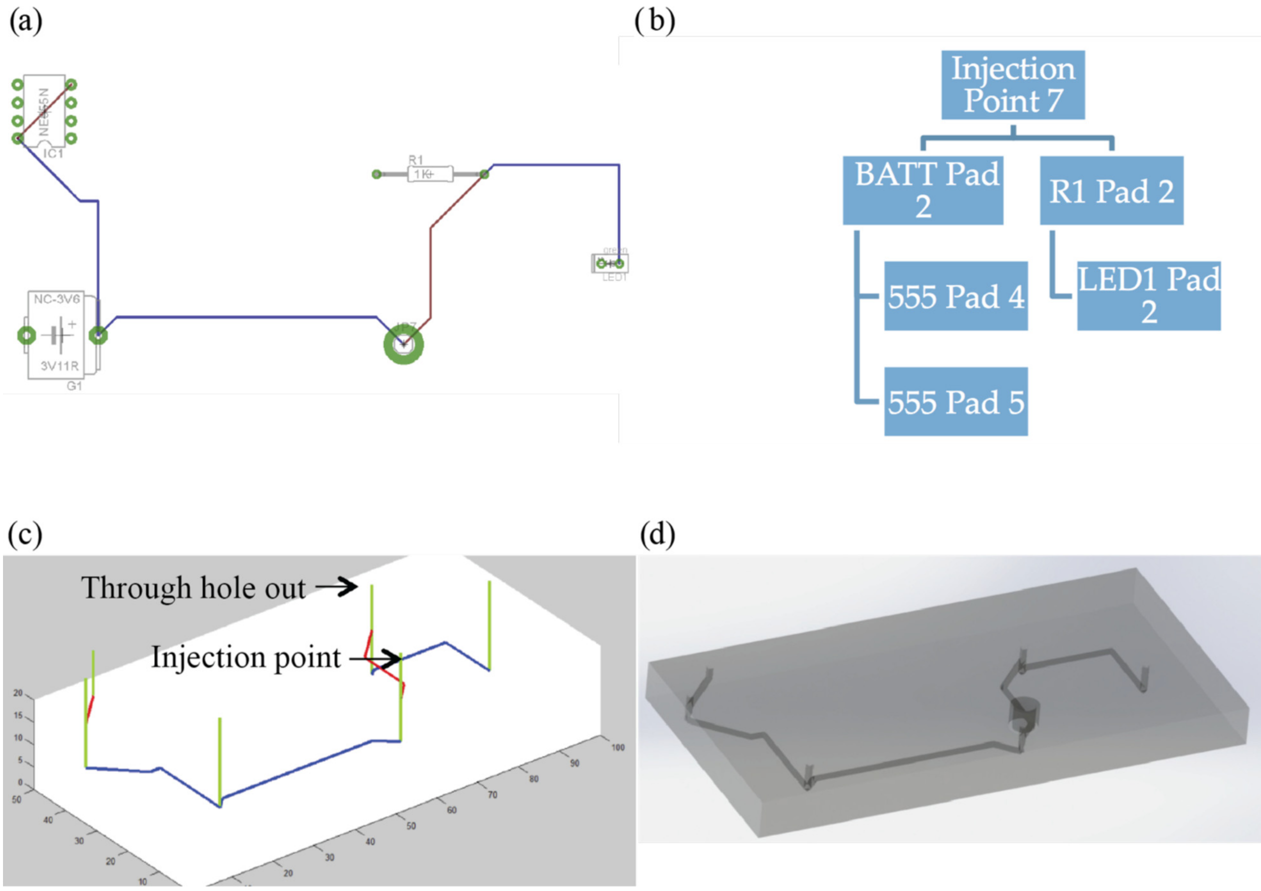

Fig. 7 The complete process of conversion of a single trace from circuit board CAD software (EAGLE PCB) to the equivalent 3D printed part with channels ready for injection: (*a*) the EAGLE PCB representation of a single trace of the circuit, (*b*) the extracted tree representation of the trace starting at the injection point and ending at each component pin location, (*c*) a plot of the extracted tree with layer depths and channel diameters specified, and (*d*) the conversion of the circuit trace tree representation to STL format using the programmatic solid modeling language and software OPENSCAD

A key challenge for injectable circuits is the desire to have the injected metal reach all the pins of a particular channel simultaneously. Not only will this limit spillage at the terminals of the electronic components but also will prevent undesired shorts between components. This is achieved by algorithmically determining the appropriate channels diameters for each section along the injection path to either allow or restrict flow, thus achieving the objective.

The .BRD file format from EAGLE PCB is a human readable extensible markup language (XML) file. Using the XML parsing libraries provide by MATLAB the circuit board was parsed into its key features, namely (1) injection points, (2) the starting and ending coordinates and layer of each segment of an electrical trace, (3) vias between layers, and (4) through-holes connecting all layers to the component location on the surface of the board. During the circuit board design process, an additional pin location was added to each of the traces in the circuit to act as the injection point. An example of each of these features is shown in Fig. 6.

After a complete trace, or connected set of channels with equivalent electrical potential, was extracted from the .BRD file, Fig. 7(*a*), the list of board features was organized into a tree structure beginning with the injection point and branching to reach each of the component pin locations, as shown in Fig. 7(*b*). The tree was then traversed, Fig. 7(*c*), to generate a programmatic CAD representation of the circuit using the open-source OPENSCAD language[2] after which the OPENSCAD software generated an STL file, Fig. 7(*d*), suitable for use in the authors' FDM printer.

[2]www.openscad.org.

One of the most critical steps during the automated generation of channels for the RP circuit is to ensure that the injected material reaches all of the circuit component pin locations simultaneously such that spillage and unintentional shorting between traces are avoided. This is accomplished by optimizing the diameters of each of the segments of a particular trace such that the liquid metal reaches each component pin with the minimum variance in arrival time. Using the simplified fluid mechanics described in Sec. 3 and the parsed tree representation of a trace from injection to all of its component pin outlets, a simulation of the fluid flow including branching was implemented. The inputs to the simulation were the diameters and lengths of each segment within the trace, a simulation time step, the volumetric flow rate from the injection device, and the topology of the trace from injection to outlets. The output of this simulation was a set of times $\{t_k\}$ representing the times at which the fluid would begin exiting each component pin outlet hole. Then, a constrained optimization was executed, where the circuit topology was fixed and the optimization was over the channel diameters, d_p. The constraints were a minimum channel cross-sectional area of $0.8 \times 0.8\ \mathrm{mm}^2$ and a maximum cross-sectional area of $1.6 \times 1.6\ \mathrm{mm}^2$, with the optimization criterion being the minimization of the variance of $\{t_k\}$

$$\{d_\mathrm{p}^*\} = \arg\min_{\{d_\mathrm{p}\}} \mathrm{var}(\{t_k\}), \quad 0.8\,\mathrm{mm} < d_\mathrm{p} < 1.6\,\mathrm{mm} \tag{9}$$

The algorithm for simulating a single injection is given in pseudocode for in the table below and is available upon request from the corresponding author.

Injection Simulation Algorithm

Inputs: (1) Channel topology from injection point to vents
(2) Channel diameters for each circuit segment
(3) Volumetric flow rate
(4) Time step

Output: The set of times at which fluid reaches the vents, $\{t_k\}$.

Algorithm:

(1) Add the first channel segment from the injection point to the list of active channel segments.

(2) While (!all_branches_full)

(a) Determine which branches currently have fluid traveling in them (e.g., active channel segments).

(b) Update the fluid flow resistance for each filled or partially filled channel, based on Eq. (2) and the length of fluid in the channel.

(c) Update the flow rates in each channel based on the fluid divider ratios as given in Eqs. (5) and (6), calculated from the relative fluid resistance exhibited by each channel and its filled children.

(d) Update the advancing fluid head in each of the partially filled channels using Eq. (4).

(e) If the end of a channel has been reached, add the branching children to the list of active channel segments.

(f) If the fluid has reached a vent at a component pin location, add the current simulation time to the list of vent arrival times, $\{t_k\}$.

End.

This minimization ensured that we found a local minimum where the time at which the metal reached the component pin outlet holes was small.

6 Design Experiment

A variety of design experiments were conducted to validate the proposed method of printing channels into 3D printed parts with subsequent injection of liquid metal. The experiments explored a variety of expected outcomes for repeatability and quality including: (1) examining the effects of very long traces and comparing predicted and actual resistances given channel geometry and length, (2) the effects of branching and varying channel diameters along the branches, and (3) creating a test circuit using discrete components and the circuit generation algorithm described in Sec. 4.

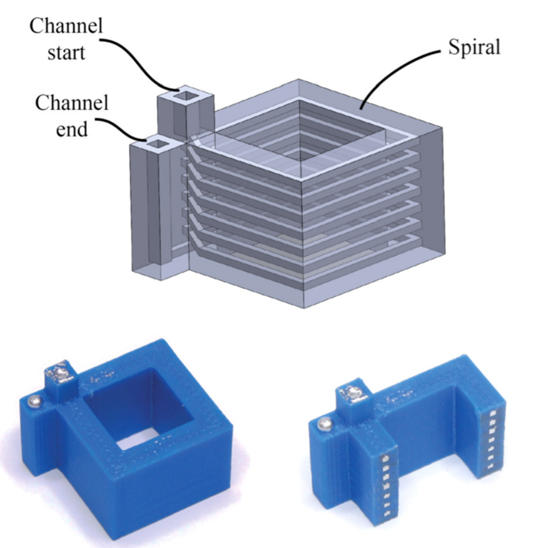

Fig. 8 A spiral-shaped trace 465 mm long was printed into a test part to demonstrate lengths at which the traces can be cast, and the ability to make three-dimensional circuits. The sectioned part shows that the trace has completely filled the channel without leakage.

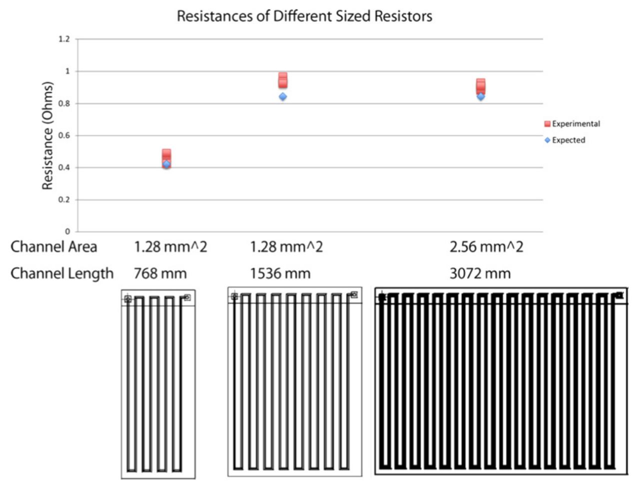

Fig. 9 The expected and actual resistance measurements for three test pieces each of three different channel cross-sectional areas and/or lengths

6.1 Long Channels. Two experiments were conducted to demonstrate the capabilities of the liquid metal injection process and to verify that the resistance of traces matched the predicted value. The first test, depicted in Fig. 8, is a long coil winding in a spiral through a square tube. This part was created to illustrate the ability to make three-dimensional traces and to test whether parts would leak when long traces were filled. The spiral measured 1.6 mm × 1.6 mm and had a total trace length of 465 mm.

The part was filled completely in a single injection attempt and was then sectioned to determine whether any internal leakage had occurred. The traces were well-defined and no flashing of metal could be seen between the layers of 3D printed material. The

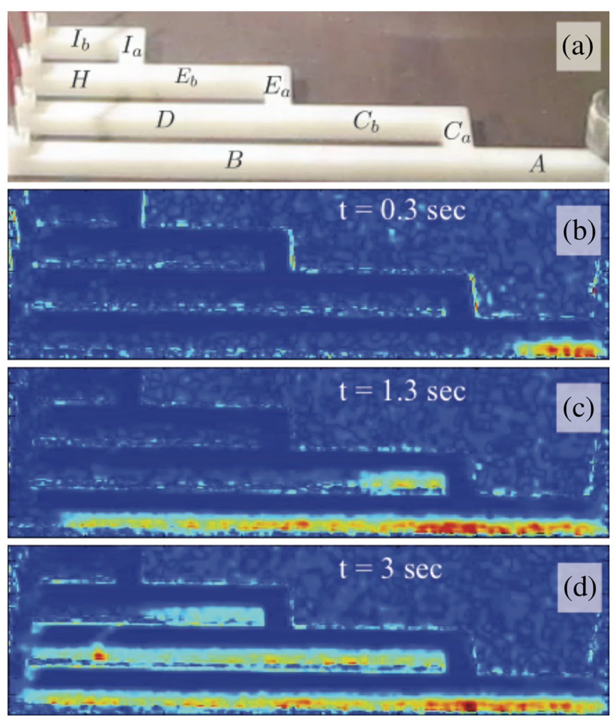

Fig. 10 The branching test piece and visual tracking of fluid advancement through background image subtraction using a visible light camera: (*a*) the branching test piece where the diameter of the channels in each of the four branches can be varied and (*b*)–(*d*) the advancing liquid metal for a single injection at three different times

spiral trace confirms that this method is viable for creating not only short traces but also potentially very long ones, such as a power or data bus running up the arm or leg of a robot. The part was cut and inspected to see if there was flashing or the beginning of flashing between adjacent layers (lower-right of Fig. 8).

In the second experiment, shown in Fig. 9, three different test pieces were printed and injected with material. The resistance predicted from Eq. (1) based on the cross-sectional area and length of the channel is plotted versus the measurement of the resistance of the three test samples. The resistance was measured using a standard three-point resistance measurement. The mean measured resistance was within 13.1%, 11.4%, and 7.3% of the predicted value for the increasing channel length. In all cases, the measured value was higher than the predicted value. This is not surprising as the FDM printers used to create these channels are known to undersize extremely small features. The deviation of the area of the designed channel and the actual area is printer dependent. Each researcher should identify the tendency of their particular printing method to either oversize or undersize channels as the given channel diameters. The first two test pieces, left and center in Fig. 9, had a cross-sectional area of 1.28 mm^2, while the third test piece, right, had a cross-sectional area of 2.56 mm^2.

6.2 Branching Channels. To explore the effects of channel diameter on the travel of liquid metal through circuits, a branching test piece, shown in Fig. 10(*a*) was created. The advancing head of the liquid metal was tracked in each channel by capturing video of the part during injection and performing background image subtraction to accentuate the visible difference between an empty and full channel. An example trial at three different time intervals during a single insertion is shown in Figs. 10(*b*)–10(*d*).

The visible-light camera technique used to track the advancing head of the fluid in each channel can only detect fluid flow in the channels aligned horizontal to the camera because it relies on light passing through the thin ABS parts to distinguish between an empty and full channel. So, when comparing the simulated and experimental results, we only track the position of the fluid head in each channel as indicated in Fig. 11(*a*). Occasionally a bubble would be trapped in the pathway of the injection apparatus, thus causing delays during the infusion of liquid metal. Figure 11(*b*) shows a typical good injection where the channels were completely filled at the expected final time based on the total volume of all the channels and the volumetric flow rate from the injection apparatus. Figure 11(*c*) shows a problematic injection where a bubble caused a delay during injection. Experimentally, the existence of a bubble appeared to only cause a delay in the injection process and did not otherwise cause large deviations in how the fluid split and advanced to the exit vents. The demonstration injections in Fig. 11 were done with an unoptimized channel cross-sectional area of 1.6×1.6 mm^2.

The simulated and actual injections were compared for three different kinds of channel diameters: (1) constant for all channels, (2) increasing for each successive channel, and (3) optimized based on the simulations using the algorithm from Sec. 4. Figure 12(*a*) shows the simulation (dashed lines) and experimental result (solid lines) for the branching test piece where all channels were 1.6×1.6 mm^2 in cross-sectional area. The fact that the earlier branches fill more quickly than the simulation suggests may indicate that the pressure drops due to branching, turns, and diameter

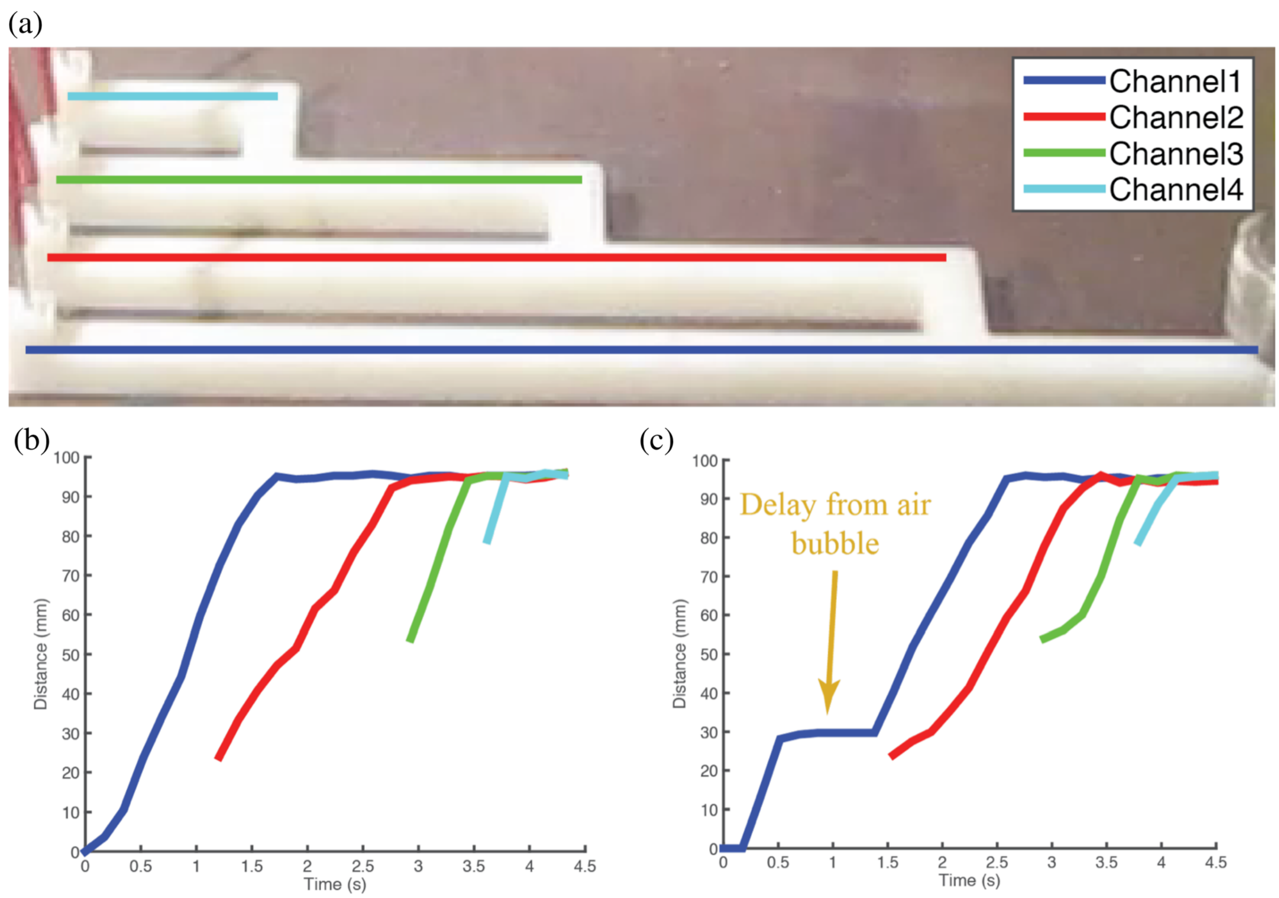

Fig. 11 Injection experimental results including potential error conditions: (*a*) the branching test piece used to compare injection simulations with experimental results, (*b*) a typical good injection, and (*c*) a problematic injection where an air bubble had formed in the injection apparatus, thus causing a delay when the bubble reached the injection point. Because the visual fluid tracking only allowed us to tracked fluid in the horizontal direction, only the position of the fluid head in each horizontal channel is plotted.

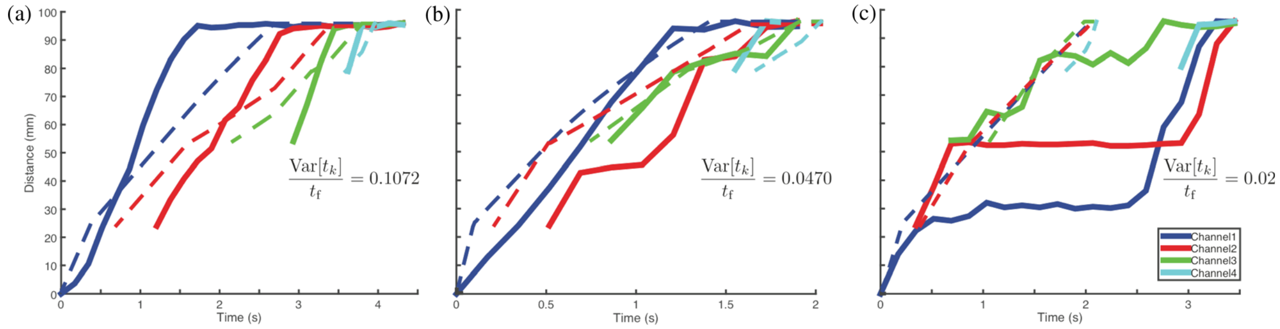

Fig. 12 Injection simulations (dashed lines) and experimental results (solid lines): (*a*) all channels are 1.6 × 1.6 mm², (*b*) the first channel is 0.8 ×0.8 mm² and each successive channel has 2-, 3-, and 4-times the cross-sectional area, and (*c*) the optimized channel diameters. Note that in the case of the optimized channel diameters that a bubble in the injection pathway caused a delay during injection, but that the variance in final arrival time was less than the nonoptimized cases despite the delay.

changes should be incorporated into the simulation. Figure 12(*b*) shows simulation results where the smallest channel has a cross-sectional area of $A = 0.8 \times 0.8$ mm^2 and each successive channel has a cross-sectional area of 2*A*, 3*A*, and 4*A*, respectively. Finally, the branching test piece with optimized channel diameters is shown in Fig. 12(*c*) ($d = $(1.177, 0.970, 1.474, 1.474, 0.919, 1.348, 1.348, 1.199, 1.168, 1.168) mm, where the segment definitions are given in Fig. 10(*a*) as segments *A* through I_b). This trial, despite experiencing a delay due to a bubble during injection, indicates that optimizing the channel diameters is able to effectively ensure that all channels reach their outlets with the minimum variance in arrival time, compared to the nominal (not optimized) diameters. In each case, the variance of the arrival times normalized by the final completion time is shown in Fig. 12. The variance is normalize because the difference in channel diameters, and thus the difference in total volume of the channels combined, affects the time at which are channels are filled when given the same input flow rate.

In all cases, because of the difference in arrival times at the component hole locations, even in the fully optimized case, there is a minimal spillage that needs to be cleaned up. In our case, we designed small risers at each of the component points in the automated STL generation. This allowed the spillage to maintain isolation between pins and minimal scraping with a utility knife and putty knife was necessary to clean the spillage from the surface of the part.

6.3 555 Timer Circuit. The final, more difficult demonstration part was an example circuit built without a PCB, depicted in Fig. 1. For example, we chose a relaxation oscillator—a common circuit using a variety of discrete component such as resistors, capacitors, light emitting diode (LED), and integrated circuit chips. The part count was low enough to complete with a simple two layer board, yet complicated enough to be a nontrivial demonstration. The circuit was first designed in EAGLE PCB using standard schematic capture (Fig. 1(*a*)) where the only additional circuit component that would not normally be included in a schematic design is the isolated pins representing the injection points. This schematic was used to generate a board layout (Fig. 1(*b*)), and the autorouting constraints were modified for a minimum of 80 mil trace-to-trace distance to ensure the minimum number of contours could be achieved in the printed part. The resulting .BRD file from the board layout process was parsed, the channel sizes optimized, and the 3D printed part was generated in STL format. All of the metal traces were injected into a block of printed ABS, and each trace contained multiple holes for the insertion of component leads.

The population of the circuit, shown in Fig. 1(*c*), was done after the complete injection process. This was done to allow testing of the circuit for continuity and unwanted shorts without the discrete electronic components in place. After continuity testing, the discrete components were put in place by heating the pins of the component and causing localized melting of the Cerrolow 136.

The oscillator worked as designed, blinking an LED on and off when power was connected to the power and ground pins. This simple circuit was chosen for the ease of verification. The DIP socket could also be used to place small microprocessors throughout a robot, to act as bus interfaces for smaller sensors, or to sample analog signals.

6.4 Summary. These demonstration parts show that the basic design goals of the liquid metal injection process are sufficient to construct traces that are both long and complex inside a rapid-prototyped part. The practical process problems such as spillage due to uneven arrival times at the outlets and leakage between channels can be avoided if the process is properly controlled, and the potential of these techniques is clear. The demonstration parts were kept simple to focus primarily on the fabrication process, but in the near future, more ambitious applications such as touch sensors for robot fingers will be developed.

7 Conclusions and Future Work

The overall goal of this work is the development and dissemination of methods for improving the performance of rapidly prototyped robots. The automated method presented here uses traditional circuit prototyping techniques and translates the results into 3D model appropriate for printing using a variety of rapid prototyping methods. As one of the revolutionary aspects of AM is the ability to create structures and components that cannot be manufactured using traditional fabrications techniques, RP circuits also have the potential to be transformative in allowing sensing, actuation, and other electronics to be seamlessly incorporated into mechanical components. This particular approach is much less time-consuming than manually wiring and inserting a large number of sensors into a rapidly prototyped device and has the advantage over many other existing RP circuit techniques in that is allows multilayered designs. Considering the benefits reaped so far by experimental roboticists from rapid prototyping technology, the development of integrated rapid-prototyped circuits is a logical next step.

A number of future improvements to this technique are currently under development, and will be forthcoming shortly.

Attachment to PCBs. It is common to connect a large number of PCBs to a bus providing power and communication. One possible application of injected liquid metal wiring is to attach, power, and network circuit boards held in recesses on a solid part. This level of modularity would allow easy assembly of generic sensor nodes onto reconfigurable printed robots, and make distribution of open, modifiable CAD files for robots more practical and feasible.

Manipulating of Surface Tension. The degree to which liquid metals appear to wet a surfaces is determined largely by surface chemistry [28]. Chemicals on the surface will either oxidize the metal, increasing apparent wetting, or to reduce the metal, decreasing apparent wetting. Because sodium hydroxide is often used to dissolve support material from FDM parts, it is relatively straightforward to coat a printed part in a substance that will repel the liquid metal. This may be a way to reduce the potential for leaks and short circuits inside traces. More recent techniques to control the interfacial energy include both texturing of the surface [29] and active control through applied voltages [30]. The former could be quite challenging during the 3D printing process, but could be implemented as a postprint, pre-injection process through chemical treatment of the channels that have been formed. The latter method of applied voltages could be implemented more easily by modifying the injection apparatus to allow controlled voltages to be applied to the liquid metal as it is injected into the channels.

Direct Interface to Surface Mount Components. It may be possible to push the trace size and spacing down to widths where the largest standard surface mount components, such as SOIC packages, can be directly integrated into printed components. One long-term objective is the ability to directly interface to MEMS barometric pressure sensors, so that the contact detection circuits used in the iHY hand and described in Ref. [9] can be implemented in very constrained geometries where it may not be possible to package a circuit board.

At present, the state of the art in rapidly prototyped robots consists of great mechanisms packaged with more or less conventional electronics mounted on circuit boards and connected with wires. In order to move past this, better methods for connecting electronic components to printed mechanical components are needed. This paper has shown that liquid metal injection is feasible and has described a set of process parameters that enable anyone with a FDM printer to make printed ABS circuits using existing circuit design tools.

Acknowledgment

The authors would like to thank Alejandro Carrillo, Gerardo Carranza, and Tom Bu for their assistance in process development, testing, and experiment hardware. This work was supported by DARPA grant no. D13AP00056.

References

[1] Merz, R., Prinz, F. B., Ramaswami, K., Terk, M., and Weiss, L., 1994, *Shape Deposition Manufacturing*, Engineering Design Research Center, Carnegie Mellon University, Pittsburgh, PA.
[2] Laliberte, T., Gosselin, C. M., and Cote, G., 2001, "Practical Prototyping," IEEE Rob. Autom. Mag., **8**(3), pp. 43–52.
[3] Quigley, M., Asbeck, A., and Ng, A., 2011, "A Low-Cost Compliant 7-DOF Robotic Manipulator," IEEE International Conference on Robotics and Automation, pp. 6051–6058.
[4] Ma, R. R., Odhner, L. U., and Dollar, A. M., 2013, "A Modular, Open-Source 3D Printed Underactuated Hand," IEEE International Conference on Robotics and Automation, pp. 2737–2743.
[5] Malone, E., and Lipson, H., 2007, "Fab@Home: The Personal Desktop Fabricator Kit," Rapid Prototyping J., **13**(4), pp. 245–255.
[6] Cham, J. G., Bailey, S. A., Clark, J. E., Full, R. J., and Cutkosky, M. R., 2002, "Fast and Robust: Hexapedal Robots Via Shape Deposition Manufacturing," Int. J. Rob. Res., **21**(10–11), pp. 869–882.
[7] Dollar, A. M., Wagner, C. R., and Howe, R. D., 2006, "Embedded Sensors for Biomimetic Robotics Via Shape Deposition Manufacturing," The First IEEE/RAS-EMBS International Conference on Biomedical Robotics and Biomechatronics (BioRob 2006), Pisa, Italy, Feb. 20–22, pp. 763–768.
[8] Odhner, L. U., Jentoft, L. P., Claffee, M. R., Corson, N., Tenzer, Y., Ma, R. R., Buehler, M., Kohout, R., Howe, R. D., and Dollar, A. M., 2014, "A Compliant, Underactuated Hand for Robust Manipulation," Int. J. Rob. Res., **33**(5), pp. 736–752.
[9] Tenzer, Y., Jentoft, L. P., and Howe, R. D., 2014, "Inexpensive and Easily Customized Tactile Array Sensors Using MEMS Barometers Chips," IEEE Robot. Autom. Mag. (in press).
[10] Czyżewski, J., Burzyński, P., Gaweł, K., and Meisner, J., 2009, "Rapid Prototyping of Electrically Conductive Components Using 3D Printing Technology," J. Mater. Process. Technol., **209**(12–13), pp. 5281–5285.
[11] Leigh, S. J., Bradley, R. J., Purssell, C. P., Billson, D. R., and Hutchins, D. A., 2012, "A Simple, Low-Cost Conductive Composite Material for 3D Printing of Electronic Sensors," PLoS One, **7**(11), p. e49365.
[12] Periard, D., Malone, E., and Lipson, H., 2007, "Printing Embedded Circuits," 18th Solid Freeform Fabrication Symposium, Austin TX, Aug. 6–8, pp. 503–512.
[13] Bare Conductive, 2013, "Bare Paint Technical Data Sheet," Bare Conductive, London, UK, accessed Feb. 7, 2014, http://www.bareconductive.com/wp-content/uploads/2013/11/2013.TechnicalDataSheet_ElectricPaint.pdf
[14] Kawahara, Y., Hodges, S., Cook, B. S., Zhang, C., and Abowd, G. D., 2013, "Instant Inkjet Circuits: Lab-Based Inkjet Printing to Support Rapid Prototyping of UbiComp Devices," ACM International Joint Conference on Pervasive and Ubiquitous Computing (UbiComp '13), Zurich, Switzerland, Sept. 8–12, pp. 363–372.
[15] van Osch, T. H. J., Perelaer, J., de Laat, A. W. M., and Schubert, U. S., 2008, "Inkjet Printing of Narrow Conductive Tracks on Untreated Polymeric Substrates," Adv. Mater., **20**(2), pp. 343–345.
[16] Ladd, C., So, J.-H., Muth, J., and Dickey, M. D., 2013, "3D Printing of Free Standing Liquid Metal Microstructures," Adv. Mater., **25**(36), pp. 5081–5085.
[17] Fassler, A., and Majidi, C., 2013, "3D Structures of Liquid-Phase GaIn Alloy Embedded in PDMS With Freeze Casting," Lab Chip, **13**(22), pp. 4442–4450.
[18] Siegel, A. C., Bruzewicz, D. A., Weibel, D. B., and Whitesides, G. M., 2007, "Microsolidics: Fabrication of Three-Dimensional Metallic Microstructures in Poly(dimethylsiloxane)," Adv. Mater., **19**(5), pp. 727–733.
[19] Dickey, M. D., Chiechi, R. C., Larsen, R. J., Weiss, E. A., Weitz, D. A., and Whitesides, G. M., 2008, "Eutectic Gallium-Indium (EGaIn): A Liquid Metal Alloy for the Formation of Stable Structures in Microchannels at Room Temperature," Adv. Funct. Mater., **18**(7), pp. 1097–1104.
[20] Jillek, W., and Yung, W. K. C., 2004, "Embedded Components in Printed Circuit Boards: A Processing Technology Review," Int. J. Adv. Manuf. Technol., **25**(3–4), pp. 350–360.
[21] Espalin, D., Muse, D. W., MacDonald, E., and Wicker, R. B., 2014, "3D Printing Multifunctionality: Structures With Electronics," Int. J. Adv. Manuf. Technol., **72**(5–8), pp. 963–978.
[22] MacDonald, E., Salas, R., Espalin, D., Perez, M., Aguilera, E., Muse, D., and Wicker, R. B., 2014, "3D Printing for the Rapid Prototyping of Structural Electronics," IEEE Access, **2**, pp. 234–242.
[23] Lopes, A. J., MacDonald, E., and Wicker, R. B., 2012, "Integrating Stereolithography and Direct Print Technologies for 3D Structural Electronics Fabrication," Rapid Prototyping J., **18**(2), pp. 129–143.
[24] DeNava, E., Navarrete, M., Lopes, A., Alawneh, M., Contreras, M., Muse, D., Castillo, S., MacDonald, E., and Wicker, R., 2008, "Three-Dimensional Off-Axis Component Placement and Routing for Electronics Integration Using Solid Freeform Fabrication," Solid Freeform Fabrication Symposium, The University of Texas at Austin, Austin TX, Aug. 4–6, pp. 362–369.
[25] Stratasys, 2013, "ABSplus^{TM}-P430," technical data sheet, Stratasys, Ltd., Eden Prairie, MN, accessed Feb. 7, 2014, http://www.stratasys.com/~/media/Main/Secure/MaterialSpecsMS/Fortus-Material-Specs/Fortus-MS-ABSplus-01-13-web.ashx
[26] Bolton Metal Products, 2013, "Bolton Metals Specifications," Bolton Metal Products Co., Bellefonte, PA, accessed Feb. 7, 2014, http://www.boltonmetalproducts.com/Specifications.html
[27] NFPA, 2008, "National Electrical Code 2008," National Fire Protection Association, Quincy, MA.
[28] Xu, Q., Oudalov, N., Guo, Q., Jaeger, H. M., and Brown, E., 2012, "Effect of Oxidation on the Mechanical Properties of Liquid Gallium and Eutectic Gallium-Indium," Phys. Fluids, **24**(6), p. 063101.
[29] Doudrick, K., Liu, S., Mutunga, E. M., Klein, K. L., Damle, V., Varanasi, K. K., and Rykaczewski, K., 2014, "Different Shades of Oxide: From Nanoscale Wetting Mechanisms to Contact Printing of Gallium-Based Liquid Metals," Langmuir, **30**(23), pp. 6867–6877.
[30] Khan, M. R., Eaker, C. B., Bowden, E. F., and Dickey, M. D., 2014, "Giant and Switchable Surface Activity of Liquid Metal Via Surface Oxidation," Proc. Natl. Acad. Sci. U. S. A., **111**(39), pp. 14047–14051.